This article has been accepted for publication in a future issue of this journal, but has not been fully edited. Content may change prior to final publication. Citation information: DOI 10.1109/ACCESS.2021.3058149, IEEE Access

Research on micro-CL geometric errors

Jiajun Zhang[1,2], Liu Shi[2,3], Cunfeng Wei[2,3], Baodong Liu[2,3], and Biao Wei[1],

[1]The Key Laboratory of Opto-electronic Technology and Systems, Ministry of Education, Chongqing University, Chongqing 400044, China
[2]Beijing Engineering Research Center of Radiographic Techniques and Equipment, Institute of High Energy Physics, Chinese Academy of Sciences, Beijing 100049, China
[3]School of Nuclear Science and Technology,University of Chinese Academy of Sciences, Beijing 100049, China

Corresponding author: Baodong Liu (E-mail: liubd@ihep.ac.cn).

Corresponding author: Biao Wei (E-mail: weibiao@cqu.edu.cn).

In this work, Jiajun Zhang and Baodong Liu was sponsored by National Key R&D Program of China No. 2017YFF0107201, Cunfeng Wei were sponsored by CAS Interdisciplinary Innovation Team, Project No. JCTD-2019-02.

ABSTRACT Computed laminography (CL) is a nondestructive testing technique for planar objects. It has been applied in applications like printed circuit board inspection and paleontological fossils research. However, the CL system calibration is a challenging task for complex mechanical structure and many degrees of freedom. To evaluated the influence of geometric errors, a new-type microscopic CL (micro-CL) with different kinds of geometric errors was simulated. The results can guide the installation and calibration of a micro-CL scanner.

INDEX TERMS Computed laminography, geometric errors analysis, simulation

I. INTRODUCTION

CL is widely applied in the nondestructive testing of printed circuit boards, biological fossils or solar panels and other planar objects[1]. In medical applications, CL technology has been applied to breast diagnosis[2]. In addition to the conventional laboratorial X-ray source, Helfen *et al*[4] also reported on the implementation of CL with neutron radiation and synchrotron radiation. Furthermore, Fisher *et al*[7] showed how to realize CL scanning on conventional industrial laboratory micro-CT without specialist equipment. Some studies[6] have proven that CL can produce higher resolution and quality images than computed tomography (CT) in limited angle scan.

System geometric accuracy which affects the quality of imaging is very important for a CT or CL system. In addition, the evaluation of errors is also important in the measurement process[8]. Many works have done a lot of research on the error effects of CT system. Kruth *et al*[9] and Hiller *et al*[10] conducted detailed studies on the influence of X-ray source drift on reconstructed images. Kumar *et al*[11] simulated the influence of positioning errors of each part of a CT system on measurement. Wenig *et al*[12] observed and analyzed the effect of rotation errors of the detector in CT systems. In a review literature, Dewulf *et al*[13] summarized various errors and relevant calibration methods of CT system. Regarding error research of CL, Yang *et al*[14] have done a lot of work, and proposed some calibration methods for slant angle error of CL[15].

A micro-CL system was developed by the Institute of High Energy Physics of the Chinese Academy of Sciences[1]. It has complex geometry structure and many degrees of freedom. In order to obtain the accurate reconstructed results, the actual system geometry need to be consistent with the designed geometry as much as possible. For the micro-CL structure, in addition to the inherent error of mechanical accuracy, the possible errors include: the positioning error of the X-ray source in three-dimensional motion direction, the positioning error of the sample caused by the movement of two-dimensional stage, the angle error and offset of the detector plane.

The goal of this study is to analyze the influence of above errors through computer simulation, so as to find out the acceptable error limit. Hope to guide the actual geometry calibration work

The simulation tool used in this study is the All Scale Tomographic Reconstruction Antwerp (Astra) Toolbox[16], which is an open source tomographic reconstruction toolbox based on high-performance GPU. It is developed and maintained by iMinds-Vision Laboratory and Antwerp University. One of the features of Astra Toolbox is that it supports arbitrary scanning trajectory and can set scanning geometry freely[16].

This paper is mainly divided into two parts. Section 2 is the theoretical derivation, which describe the geometric structure and error representation of the studied system. In Section 3, some results and analysis of simulation experiments are presented. Finally, the whole research results are summarized.

II. Architecture of the micro-CL scanner

As shown in Fig.1(a), the mechanical composition of the micro-CL includes an X-ray source, a C-arm, a planar detector and a two-dimensional moving platform. The C-arm is located above the platform and can rotate around the rotating axis, which is perpendicular to the two-dimensional moving platform. The detector is mounted on the C-arm and can move along the C-arm. The X-ray source is fixed under the motion platform, and its focal spot lies on the rotating axis and is located at the center of the sphere corresponding to the C-arm arc. The angle between the line from the X-ray focal spot to the detector center and the central rotation axis is called the detector deflection angle, as shown in α in Fig.1(b).

The coordinate system of the micro-CL system is shown in Fig.1(b). We assume that the detector, represented by D, rotates anticlockwise around Z axis, and the X-ray focal spot S is located on the negative half axis of Z axis. The detector plane is perpendicular to the central ray. The plane where the object center P located is XOY plane. The point O is the origin of the whole space coordinate system. The angle between OP and Y axis is β, which is called scanning angle. Points P and D move synchronously to keep points S, P, D collinear. The coordinate system is defined as Global Coordinate System (GCS).

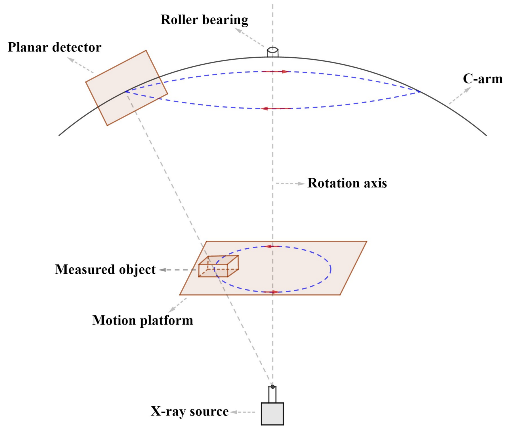

(a) Micro-CL scanning structure diagram

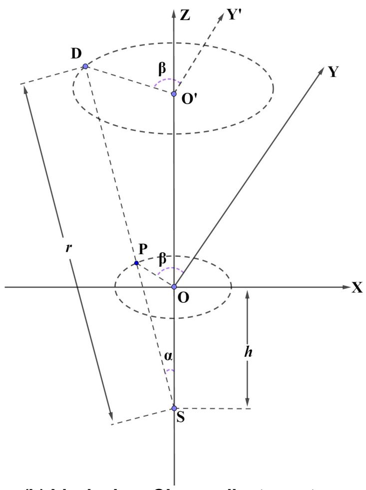

(b) Ideal micro-CL coordinate system

FIGURE 1. Micro-CL diagram. (a) micro-CL scanning structure diagram; (b) ideal micro-CL coordinate system.

Let the distance from the X-ray focus spot to XOY plane $SO=h$, the distance from the X-ray focus spot to the detector center $SD=r$. In ideal case, the coordinates of each part of the micro-CL in GCS are as follows

$$\left(0,0,-h\right)^{T}, \tag{1}$$

$$\left(-h\cdot\tan\alpha\cdot\sin\beta, h\cdot\tan\alpha\cdot\cos\beta, 0\right)^{T}, \tag{2}$$

$$\left(-r\cdot\sin\alpha\cdot\sin\beta, r\cdot\sin\alpha\cdot\cos\beta, r\cdot\cos\alpha-h\right)^{T}, \tag{3}$$

where (1) is the coordinate of X-ray focus spot S, (2) is the coordinate of object center P, (3) is the coordinate of detector center D.

A. Position errors of x-ray source and object

Due to installation errors, the position of the X-ray focal spot may have errors in X-Y-Z directions which can be expressed as Δx_S, Δy_S, Δz_S, respectively. Considering these errors, the coordinates of the ray source can be expressed as

$$\left(\Delta x_s, \Delta y_s, -h+\Delta z_s\right)^{T}. \tag{4}$$

In a scanning process, the object is moving in XOY plane with the two-dimensional motion platform, and get a circle trajectory. The position error of the object can be decomposed into X and Y direction. Considering the random position errors, the position of P with the i-th scanning angle in GCS can be express as

$$\left(-h\cdot\tan\alpha\cdot\sin\beta+\Delta x_p^i, h\cdot\tan\alpha\cdot\cos\beta+\Delta y_p^i, 0\right)^{T}, \tag{5}$$

where Δx_p^i and Δy_p^i are the errors along X axis and Y axis.

These two components are random values that vary with the scanning angle.

B. Position errors of detector

The errors of detector plane in the micro-CL system are mainly as follows: (1) Random errors of motion when the detector moving around the rotating axis; (2) Offset of the detector center; (3) The slant angle error, tilt angle error and skew angle error of the detector plane[18].

Considering the random position errors, with the i-th scanning angle, the coordinate of the detector center D in (3) becomes

$$\left(-r\cdot\sin\alpha\cdot\sin\left(\beta+\Delta\beta^i\right), r\cdot\sin\alpha\cdot\cos\left(\beta+\Delta\beta^i\right), r\cdot\cos\alpha-h\right)^{T}. \tag{6}$$

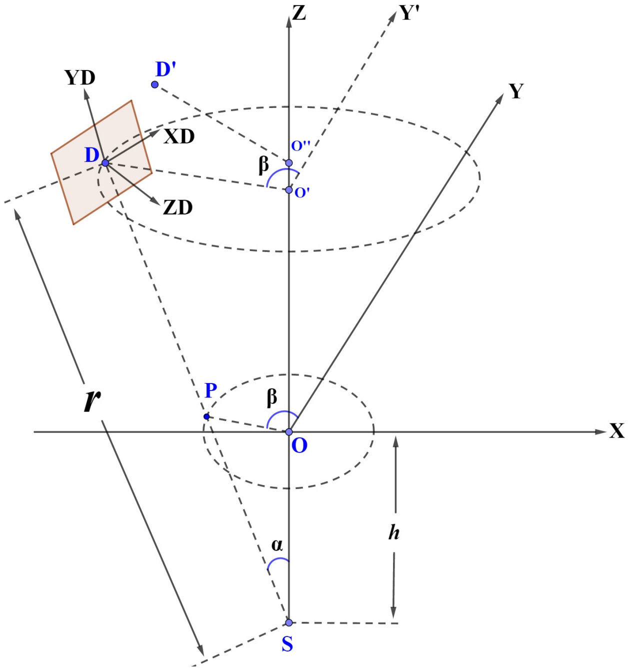

FIGURE 2. Schematic diagram of geometric coordinate system based on actual micro-CL structure

As shown in Fig.2, we take the detector plane center *D* as the origin, and set the horizontal axis, longitudinal axis and vertical axis of the detector plane as *XD*, *YD* and *ZD* axis respectively. We can establish a local Detector Coordinate System (*DCS*).

Influenced by various errors, the ideal coordinate of the detector center *D* moves to *D'*. The distance between *D* and *D'* is called the offset of the detector. It can be decomposed into $\omega=(\omega_1, \omega_2, \omega_3)$ along *XD*, *YD* and *ZD* axis. The *DCS* is also transformed due to the influence of angle errors. The coordinate system with *D'* as the origin is called real *DCS* (*RDCS*) whose three coordinate axes are *XD'*, *YD'*, *ZD'*.

Let the angle error of the detector plane rotating around *YD* axis as slant angle error φ, rotating around *XD* axis as tilt angle error θ and rotating around *ZD* axis as skew angle error γ.

The local coordinate system *DCS* based on the ideal detector plane can be regarded as the result of coordinate system transformation of *GCS*. This transformation is accomplished by using rotation matrices. The transformation of coordinate system usually needs the combined action of multiple rotation matrices, and it may include translation besides rotation. Both *GCS* and *DCS* are right-handed coordinate systems, so counter clockwise is the positive direction when rotating around the axis.

The transformation from *GCS* to *DCS* requires a total of two rotations and one translation. Rotate β around *Z* axis of *GCS* so that its *X* axis direction is consistent with *XD* axis, as shown in Fig.3(a). The rotation matrix is

$$M_1=\begin{pmatrix}\cos\beta & \sin\beta & 0\\ -\sin\beta & \cos\beta & 0\\ 0 & 0 & 1\end{pmatrix}. \tag{7}$$

Let the positions of *Y* axis at this time be Y_1 axis. Then rotate $(\pi\text{-}\alpha)$ around *XD* axis so that Y_1 and *Z* axes direction are consistent with *YD* and *ZD* axes, as shown in Fig.3(b). The rotation matrix is

$$M_2=\begin{pmatrix}1 & 0 & 0\\ 0 & \cos(\pi-\alpha) & \sin(\pi-\alpha)\\ 0 & -\sin(\pi-\alpha) & \cos(\pi-\alpha)\end{pmatrix}. \tag{8}$$

Combine the rotation matrix (7) and (8) to get the comprehensive rotation matrix *M*

$$M=M_2\cdot M_1=\begin{pmatrix}\cos(\beta+\Delta\beta^i) & \cos\alpha\cdot\sin(\beta+\Delta\beta^i) & \sin\alpha\cdot\sin(\beta+\Delta\beta^i)\\ \sin(\beta+\Delta\beta^i) & -\cos\alpha\cdot\cos(\beta+\Delta\beta^i) & -\sin\alpha\cdot\cos(\beta+\Delta\beta^i)\\ 0 & \sin\alpha & -\cos\alpha\end{pmatrix}^T \tag{9}$$

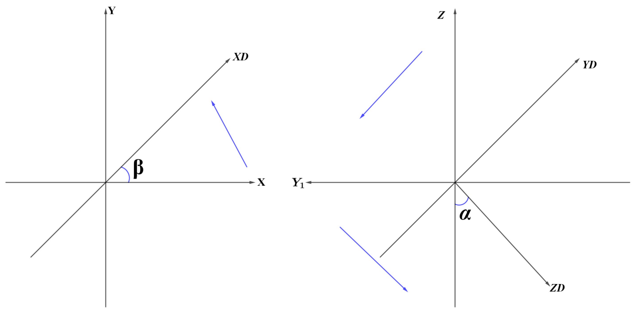

(a) (b)

FIGURE 3. ***GCS* (a) rotates *β* around *Z* axis, (b) rotates (*π-α*) around *XD* axis.**

It can be seen from Fig.2 that the translation vector from *GCS* to *DCS* is as follow

$$\overrightarrow{OD}=\left(-r\cdot\sin\alpha\cdot\sin(\beta+\Delta\beta^i),r\cdot\sin\alpha\cdot\cos(\beta+\Delta\beta^i),r\cdot\cos\alpha-h\right)^T. \tag{10}$$

In the *DCS*, the direction vector of the detector plane along three axes is matrix *v* which each column in turn represent the detector plane *XD*, *YD* and *ZD* axis direction vector. In ideal case, the direction vector expression of the detector plane in *GCS* is as follow

$$v_{GCS}=M^{-1}\cdot v=M^{-1}\cdot\begin{pmatrix}1&0&0\\0&1&0\\0&0&1\end{pmatrix}=\begin{pmatrix}\cos\beta & \cos\alpha\cdot\sin\beta & \sin\alpha\cdot\sin\beta\\ \sin\beta & -\cos\alpha\cdot\cos\beta & -\sin\alpha\cdot\cos\beta\\ 0 & \sin\alpha & -\cos\alpha\end{pmatrix}. \tag{11}$$

The coordinate system *DCS* is transformed into the *RDCS* after the effect of angle errors and offsets of the detector. The rotation operation is shown in Fig.4.

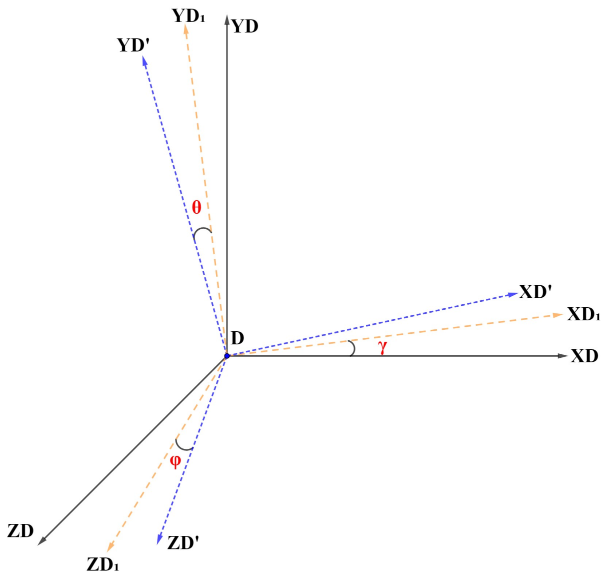

FIGURE 4. **Schematic diagram of the rotation transformation from DCS to RDCS.**

The rotation transformation can be divided into three steps:

1) Rotate γ counterclockwise around *ZD* axis. The rotation matrix is N_1;

2) Rotate θ counterclockwise around XD_1 axis. The rotation matrix is N_2;

3) Rotate φ counterclockwise around *YD'* axis. The rotation matrix is N_3.

Combine the matrices from above steps to get the comprehensive rotation matrix *N*

$$N = N_3 \cdot N_2 \cdot N_1 = \begin{pmatrix} \cos\varphi & 0 & -\sin\varphi \\ 0 & 1 & 0 \\ \sin\varphi & 0 & \cos\varphi \end{pmatrix} \begin{pmatrix} 1 & 0 & 0 \\ 0 & \cos\theta & \sin\theta \\ 0 & -\sin\theta & \cos\theta \end{pmatrix} \begin{pmatrix} \cos\gamma & \sin\gamma & 0 \\ -\sin\gamma & \cos\gamma & 0 \\ 0 & 0 & 1 \end{pmatrix}. \quad (12)$$

In *RDCS*, the direction vector of the detector plane along three axes is matrix *v'*. Then the direction vector expression of *RDCS* in *GCS* is as follow

$$v'_{GCS} = (N \cdot M)^{-1} \cdot v' = (N \cdot M)^{-1} \cdot \begin{pmatrix} 1 & 0 & 0 \\ 0 & 1 & 0 \\ 0 & 0 & 1 \end{pmatrix}. \quad (13)$$

The coordinate of the detector center *D'* in *DCS* is ω, so the coordinate of *D'* in *GCS* is

$$D' = M^{-1} \cdot \omega + \overrightarrow{OD} = M^{-1} \cdot (\omega_1, \omega_2, \omega_3)^T + \overrightarrow{OD}. \quad (14)$$

C. Simulation with Astra toolbox

In Astra toolbox, the scanning geometry always takes the measured object as the origin of the global coordinate system[16]. The geometry of the micro-CL in Astra can be expressed with Fig.5. The detector and ray source are arranged on the upper and lower sides of the object, and rotate anticlockwise around *Z* axis at the same time.

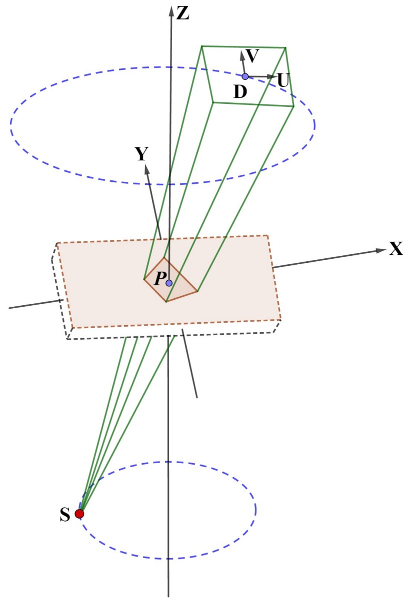

FIGURE 5. **The micro-CL scan geometry and coordinate system in Astra toolbox.**

In Astra coordinate system, the coordinate of the object is taken as the origin, and the coordinate expression of the ray source position *S'* and the detector center position *D'* with errors are as follows:

$$\begin{aligned} S' &= S - \overrightarrow{OP} \\ &= (h \cdot tan\alpha \cdot sin\beta - \Delta x_p^i + \Delta x_s, -h \cdot tan\alpha \cdot cos\beta - \Delta y_p^i + \Delta y_s, -h + \Delta z_s)^T \end{aligned} \quad (15)$$

$$D' = M^{-1} \cdot \omega + \overrightarrow{OD} - \overrightarrow{OP}$$
$$= \begin{pmatrix} \cos(\beta+\Delta\beta^i) & \cos\alpha\sin(\beta+\Delta\beta^i) & \sin\alpha\sin(\beta+\Delta\beta^i) \\ \sin(\beta+\Delta\beta^i) & -\cos\alpha\cos(\beta+\Delta\beta^i) & -\sin\alpha\cos(\beta+\Delta\beta^i) \\ 0 & \sin\alpha & -\cos\alpha \end{pmatrix} \begin{pmatrix} \omega_1 \\ \omega_2 \\ \omega_3 \end{pmatrix} + \overrightarrow{OD} - \overrightarrow{OP}. \quad (16)$$

III. Simulation experiment

In the simulation experiment, we added various errors to the projection geometry, and then the simulated phantom was projected to get the projection data with errors. By analyzing the difference between the reconstructed results from the projection with errors and without errors, the influence of geometric errors on the imaging was analyzed.

The phantom used in the simulation experiment consists of line pairs and small balls, as shown in Fig.6. Two line pairs form a group and distribute on the upper and left "petal". The width can be adjusted freely, and the minimum line pair width is one pixel size. Five small balls of the same radius are arranged in a row or a column. The radius of small balls can be adjusted freely. The gray value ranges from 0 to 1.

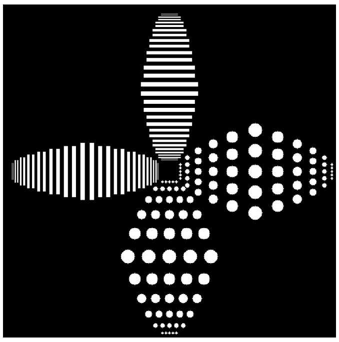

FIGURE 6. **Cross section of center layer of the phantom.**

The geometric structure of the system is shown in Fig.1. According to the actual configuration, the distance from the X-ray focal spot to the two-dimensional platform was h=7 *mm* and the distance from the detector center to the X-ray focal spot was r=340 *mm*. The detector deflection angle a=40°. The planar detector had a resolution of 580×580 with the single size was 0.0495 *mm*. The phantom size was 580×580×24. According to the calculation method of CT magnification[19], the magnification of the micro-CL system was

$$M = \frac{r\cos\alpha}{h}. \tag{17}$$

The single pixel size was about 0.0013 *mm*.

The detector and object could rotate 360° anticlockwise around Z axis, and the sampling step was 1° with a total of 360 projections. We considered here a CUDA accelerated SIRT[16] implementation for 3D data reconstruction. The iteration number was set to 100.

We used the difference map obtained by image subtraction to visually observe the influence of errors. To further evaluate the influences of errors quantitatively, we used Normalized Mean Square Distance Criterion(*NMSDC*) and Normalized Absolute Average Distance Criterion(*NAADC*)[20] to analyze the difference between reconstructed results from the projection data with errors and without errors.

$$NMSDC = \left[\frac{\sum_{u=1}^{N}\sum_{v=1}^{N}\left(t_{u,v} - l_{u,v}\right)^2}{\sum_{u=1}^{N}\sum_{v=1}^{N}\left(t_{u,v} - \bar{t}\right)^2} \right]^{\frac{1}{2}},$$

$$NAADC = \frac{\sum_{u=1}^{N}\sum_{v=1}^{N}\left|t_{u,v} - l_{u,v}\right|}{\sum_{u=1}^{N}\sum_{v=1}^{N}\left|t_{u,v}\right|}. \tag{18}$$

Where $t_{u,v}$ and $l_{u,v}$ represent respectively the pixels in the row u-th and column v-th of the reconstructed images from the projection data without errors and with errors. t is the average pixel value of the error-free reconstructed image, and the number of image pixels is $N \times N$. *NMSDC* can more sensitively reflect large errors of a few points, and *NAADC* can more sensitively reflect small errors of most points[20]. The bigger *NMSDC* or *NAADC*, the greater the difference.

Table I shows the maximum installation or mechanical error of the micro-CL. The directions of these axes are shown in Fig.1.

TABLE I
ERROR LIMITS OF THE INSTALLATION ACCURACY OF ACTUAL MICRO-CL SYSTEM

No.	Motion axis	Maximum error
1	Object moves along *X* axis	1μm
2	Object moves along *Y* axis	1μm
3	Detector rotates around *Z* axis	0.0003°
4	X-ray focal spot moves along *X* axis	3μm
5	X-ray focal spot moves along *Y* axis	3μm
6	X-ray focal spot moves along *Z* axis	3μm
7	Detector slant angle	0.2°
8	Detector tilt angle	0.2°
9	Detector skew angle	0.2°
10	Detector offset	100μm

A. The influence of single error on reconstruction results

For the simulation of the X-ray focal spot errors, the position of focal spot was perturbed by adding values ranging from 1 *μm* to 3 *μm* to three axes (*X*-*Y*-*Z*). It can be seen from Figs.7 and 8 that the errors in *X* axis and *Y* axis of the X-ray focal spot will shift the reconstructed image in the corresponding direction. This deviation will increase with the increase of errors. And the error in *Z* axis causes the reconstructed result to lose detail information, so that the image becomes blurred especially the narrowest line pairs.

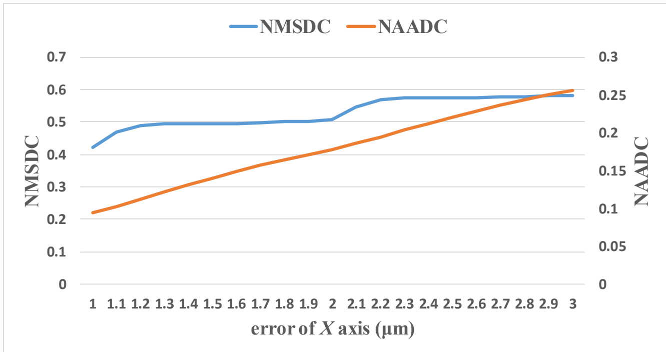

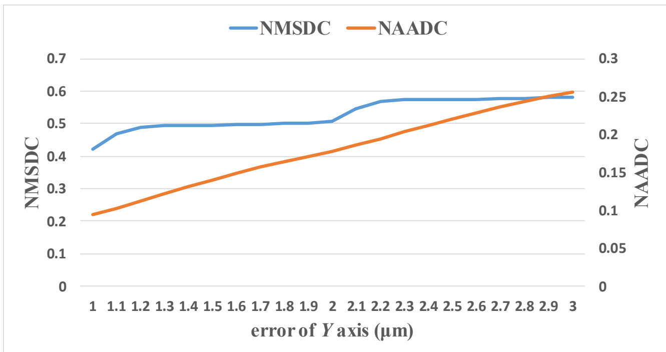

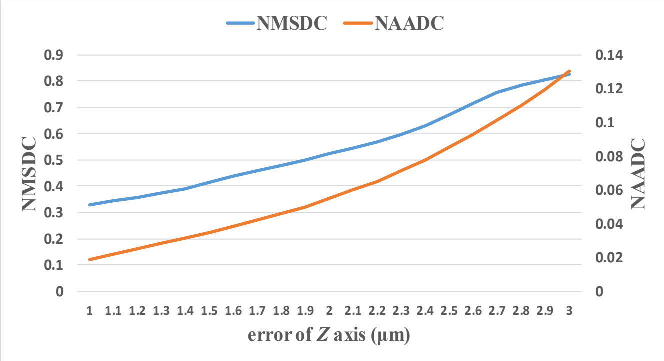

FIGURE 7. The error evaluation of the reconstructed images from the projections with X-ray focal spot errors.

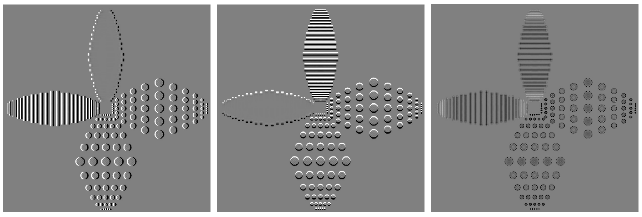

FIGURE 8. Difference map of the reconstructed images from the projection with 3 μm X-ray focal spot position error in X(left), Y(middle) and Z(right) axis. The display window is [-0.5,0.5].

The error simulation of the detector was similar to that of the X-ray focal spot. The ranges of angle (slant, tilt and skew) error and offset (along *XD* and *YD* axis) were [0°,0.2°] and [$0\mu m$,$100\mu m$]. The random motion errors generated by the detector rotating around *Z* axis were selected randomly from ±0.0003° with uniform probability distribution.

As shown in Figs.9 and 10, within the error of 0.2°, the slant angle and tilt angle error of the detector have little influence on reconstructed results, and the magnitude of *NMSDC* and *NAADC* varies from 10^{-5} to 10^{-3}. Basically, the influence of these errors can be ignored. However, reconstructed results are sensitive to the change of the detector's skew angle error. The difference map shows that the skew error makes the reconstructed image produce drag artifacts, and the image position rotate.

As shown in Figs.11 and 12, the *XD* axis offset of the detector plane blurs the contour of the line pairs and small balls. The larger the error is, the more obvious the artifacts will be. We can see from Fig.12 that the influence caused by the *YD* axis offset is similar to that caused by the *Z* axis error of the X-ray focal spot. This offset makes it difficult to distinguish the details of the reconstructed image.

It can be seen from Fig.13, the rotation motion errors of the detector in the range of ±0.0003° has little influence on reconstructed results, and can be ignored.

FIGURE 9. The angle error evaluation of the reconstructed images from the projections with the detector.

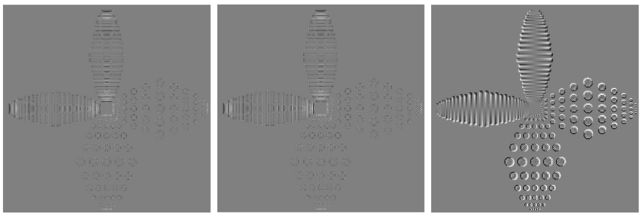

FIGURE 10. Difference map of the reconstructed images from the projection with 0.2° detector angle error in slant(left), tilt(middle) and skew(right) angle. The display window is [-0.1,0.1].

IEEE Access
Multidisciplinary ¦ Rapid Review ¦ Open Access Journal

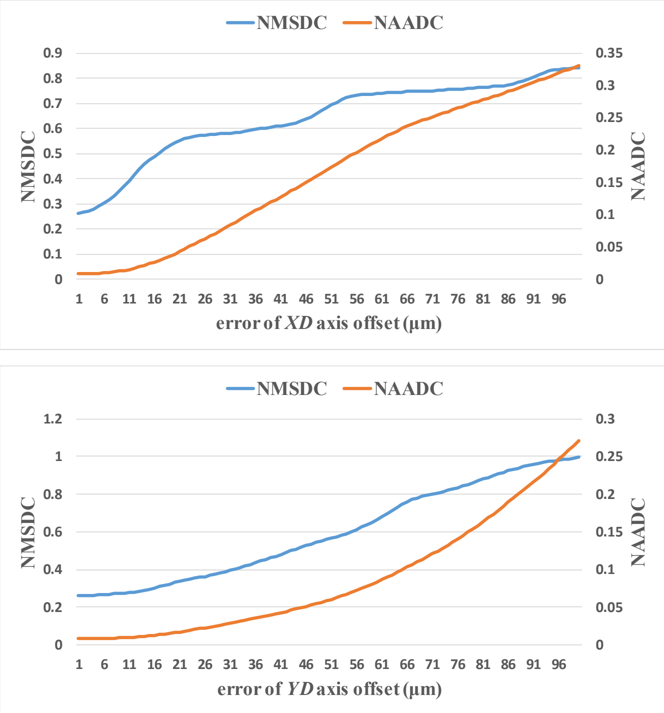

FIGURE 11. The offset error evaluation of the reconstructed images from the projections with the detector.

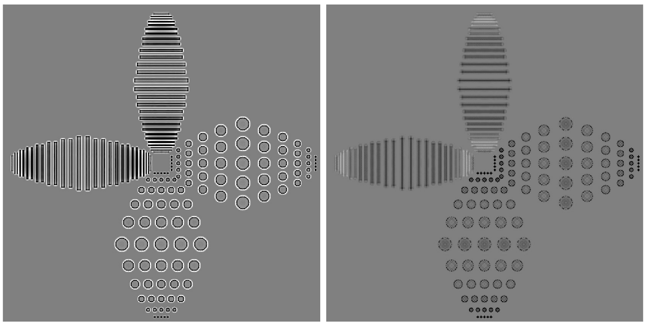

FIGURE 12. Difference map of the reconstructed images from the projection with 65 μm detector offset error in XD(left) and YD(right) axis The display window is [-0.5,0.5].

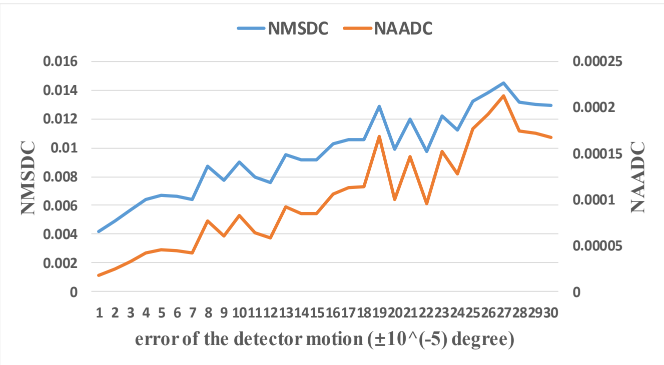

(a)

(b)

FIGURE 13. (a) The motion error evaluation of the reconstructed images from the projections with the detector, (b) Difference map of the reconstructed images from the projection with ±0.0003° random error in the detector motion. The display window is [-0.01,0.01].

The two-dimensional motion platform could move along two mutually perpendicular directions, X and Y axis. Uniform random errors ranging in ± 1 μm were added to X axis and Y axis of the object motion. As shown in Fig.14, motion errors of the object reduce the resolution of the reconstructed image. The internal gray value distribution of the balls and line pairs is uneven and edges become blurred.

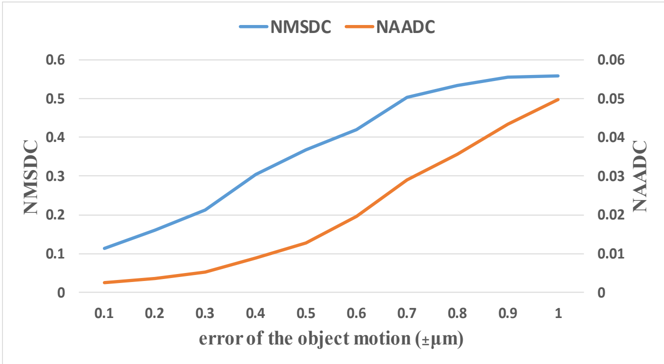

(a)

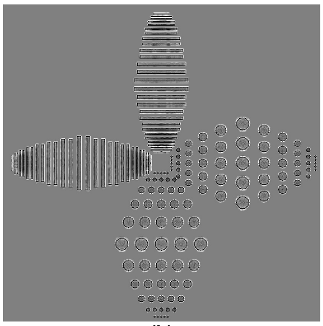

(b)

FIGURE 14. (a) The motion error evaluation of the reconstructed images from the projections with the object, (b) Difference map of the reconstructed images from the projection with ±1 μm random error in the object motion. The display window is [-0.1,0.1].

B. Comprehensive simulation experiment of all errors

Previous experiments were carried out at the same magnification. We changed the magnification of the system to observe changes in errors.

In the case of different magnification, we took all errors of the system into account and carried out the full error simulation experiment. As shown in (17), other structural parameters remained unchanged and the platform height was changed from 1 *mm* to 50 *mm* in step of 1 *mm*. The error of each part was selected randomly from Table I and the detector deflection angle was 40°. We used the error-free reconstructed image at this platform height as the original image in the difference map.

In addition, we took one set of error parameters randomly as shown in Table II to measure the reconstructed difference map at different heights, as shown in Fig.15.

It can be seen from Figs.15 and 16 that the increase of the platform height will weaken the influence of geometric errors on reconstructed results. This change is more obvious when the platform height is low. When the platform height is bigger than about 7 *mm*, the comprehensive influence of different errors on reconstructed results gradually decreases to the minimum.

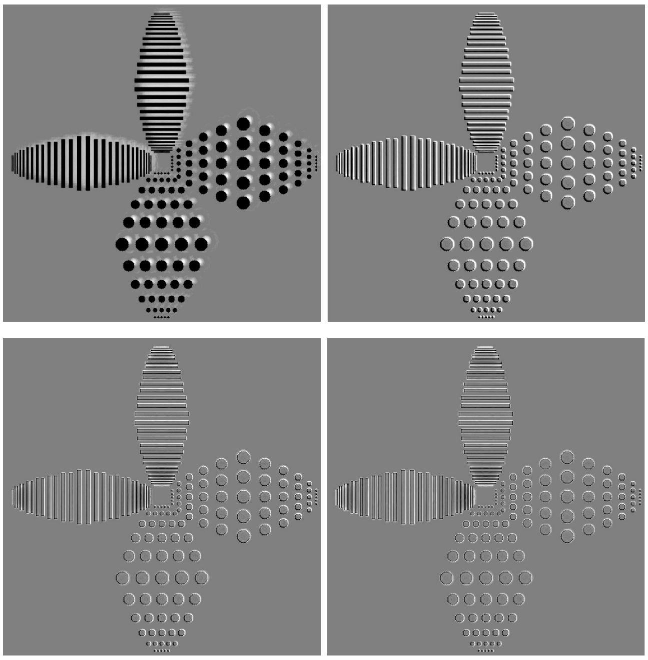

FIGURE 15. Difference map when the platform height is 1 mm, 7 mm, 25 mm and 50 mm, separately. The display window is [-0.5,0.5].

TABLE II
THE ERROR PARAMETERS

Position	Error
X axis(μm)	-1.675
Y axis(μm)	1.349
Z axis(μm)	1.457
Slant angle error(degree)	-0.096
Tilt angle error(degree)	-0.198
Skew angle error(degree)	0.114
XD axis offset(μm)	-41.932
YD axis offset(μm)	-10.624
Detector rotation error(degree)	±0.0003
Object motion error(μm)	±1

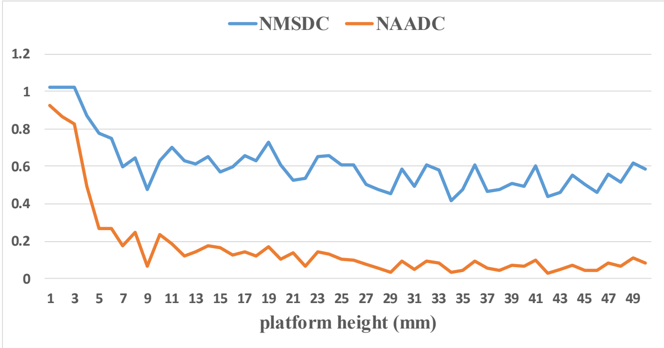

FIGURE 16. The error evaluation of the reconstructed images when the platform height is different.

Known from (17), changing the detector deflection angle will also change the magnification of the system. So we set the change range of detector deflection angle from 30° to 60° with the step size was 1°. The error of each part was selected randomly from Table I and the platform height was 7 *mm*. Similar to the previous experiment, we also used the error parameters in Table II to measure the reconstructed difference map at different deflection angles. The results were shown in Fig.17.

From the following results, it can be seen that the change of detector deflection angle has not a too obvious effect on the error influence. This effect is reflected in the evaluation index is an overall stable curve, fluctuating in a reasonable range as shown in Fig.18. As seen in (17), the influence of the detector deflection angle on the magnification is not obvious, so theoretically, the change of deflection angle has little effects on errors. The measurement results are in accord with the inference.

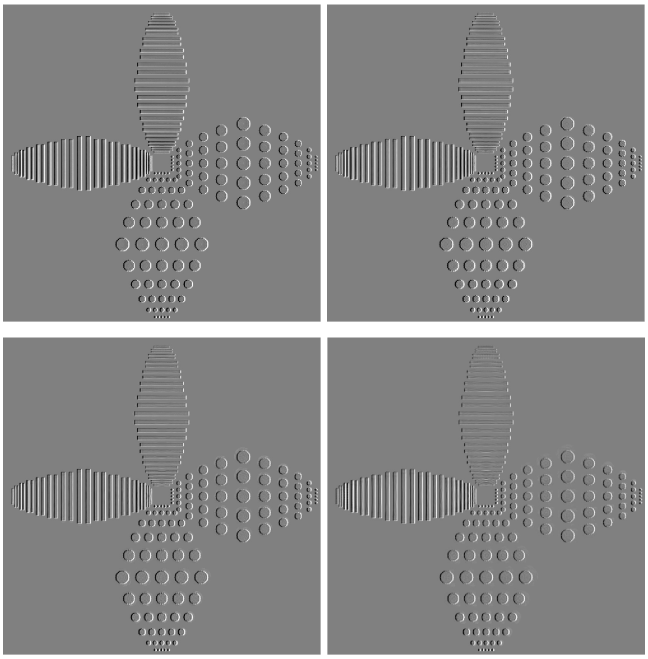

FIGURE 17. Difference map when the detector deflection angle is 30°, 40°, 50° and 60°, separately. The display window is [-0.5,0.5].

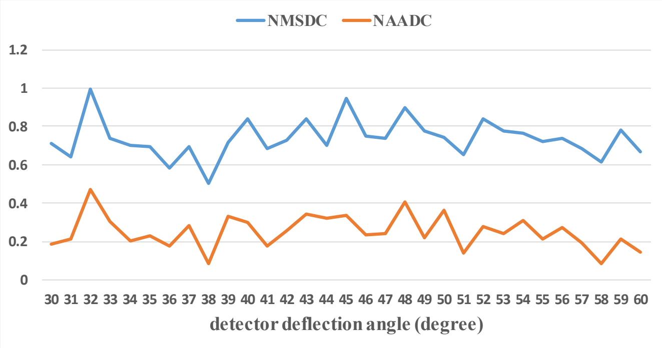

FIGURE 18. The error evaluation of the reconstructed images when the detector deflection angle is different.

IV. Conclusion

The error simulation experiments were carried out based on the micro-CL system to observe the changes of reconstructed results under the influence of different errors. At the same time, we observed and measured the influence of various errors on reconstructed results under different magnification by changing the detector deflection angle and two-dimensional platform height.

The simulation results show that within the maximum installation errors, some geometric errors like slant angle, tilt angle and motion errors of the detector have little effects on the imaging of micro-CL which can be ignored, while others need to be carefully considered, such as the X-ray focal spot drift, object motion errors, detector offset and skew angle errors. On the other hand, we have considered the influence of geometric errors under different magnification. The results show that the change of platform height has an effect on errors because it greatly changes the magnification, while errors are not sensitive to the change of detector deflection angle.

The above experimental results will have a guiding role for the mechanical installation and calibration work. However, this study only considered the influence of geometric errors under ideal conditions. In practical applications, some physical phenomena and working environment will also affect the imaging of the micro-CL, which we need to study in the future.

ACKNOWLEDGMENT

The authors gratefully acknowledge financial support to this research work from National Key R&D Program of China and experimental condition support from The Institute of High Energy Physics of the Chinese Academy of Sciences.

REFERENCES

[1] Z. H. Wei, L. L. Yuan, B. D. Liu, et al. “A micro-CL system and its applications,” *Review of entific Instruments*, vol. 88, no. 11, pp. 115107-115107, Nov. 2017, DOI: 10.1063/1.4989444.

[2] S. Ioannis. “A review of breast tomosynthesis. Part I. The image acquisition process,” *Medical Physics*, vol. 40, no. 1, pp. 014301, Jan. 2013, DOI: 10.1118/1.4770279.

[3] S. Ioannis. “A review of breast tomosynthesis. Part II. Image reconstruction, processing and analysis, and advanced applications,” *Medical Physics*, vol. 40, no. 1, pp. 014302, Jan. 2013, DOI: 10.1118/1.4770281.

[4] L. Helfen, F. Xu, H. Suhonen, P, et al. “Laminographic imaging using synchrotron radiation – challenges and opportunities,” *Journal of Physics Conference*, vol. 425, no. 19, pp. 192025, 2013, DOI: 10.1088/1742-6596/425/19/192025.

[5] L. Helfen, F. Xu, B. Schillinger, et al. “Neutron laminography—a novel approach to three-dimensional imaging of flat objects with neutrons,” *Nuclear Instruments & Methods in Physics Research*, vol. 651, no. 1, pp. 135-139, 2011, DOI: 10.1016/j.nima.2011.01.114.

[6] F. Xu, L. Helfen, T. Baumbach, et al. “Comparison of image quality in computed laminography and tomography,” *Optics Express*, vol. 20, no. 2, pp. 794-806, Jan. 2012, DOI: 10.1364/oe.20.000794.

[7] S. L. Fisher, D. J. Holmes, J. S. Jrgensen, et al. “Laminography in the lab: imaging planar objects using a conventional x-ray CT scanner,” *Measurement Science and Technology*, vol. 30, no. 3, pp. 035401-12, Feb. 2019, DOI: 10.1088/1361-6501/aafcae.

[8] S. Carmignato, A. Pierobon, P. Rampazzo, et al. “CT for Industrial Metrology – Accuracy and Structural Resolution of CT Dimensional Measurements,” *Conference on Industrial Computed Tomography (ICT)*, pp. 161–172, 2012.

[9] J. P. Kruth, M. Bartscher, S. Carmignato, et al. “Computed tomography for dimensional metrology,” *CIRP Annals - Manufacturing Technology*, vol. 60, no. 2, pp. 821-842, Dec. 2011, DOI: 10.1016/j.cirp.2011.05.006.

[10] J. Hiller, M. Maisl, and L. M. Reindl, “Physical characterization and performance evaluation of an x-ray micro-computed tomography system for dimensional metrology applications,” *Measurement ence and Technology*, vol. 23, no. 8, pp. 085404, Jun. 2012, DOI: 10.1088/0957-0233/23/8/085404.

[11] J. Kumar, A. Attridge, P. K. C. Wood, et al. “Analysis of the effect of cone-beam geometry and test object configuration on the measurement accuracy of a computed tomography scanner used for dimensional measurement,” *Measurement ence & Technology*, vol. 22, no. 3, pp. 035105, Feb. 2011, DOI: 10.1088/0957-0233/22/3/035105.

[12] P. Wenig, K. Stefan, “Examination of the Measurement Uncertainty on Dimensional Measurements by X-Ray Computed Tomography,” *European Conference on Non-Destructive Testing*, pp. 1–10, 2006.

[13] M. Ferrucci, R. Leach, C. Giusca, et al. “Towards geometrical calibration of x-ray computed tomography systems-a review,” *Measurement ence & Technology*, vol. 26, no. 9, pp. 092003-1-092003-30, Aug. 2015, DOI: 10.1088/0957-0233/26/9/092003.

[14] M. Yang, J. H. Zhang, M. D. Yuan, et al. “Calibration method of projection coordinate system for X-ray cone-beam laminography scanning system,” *NDT&E International*, vol. 52, pp. 16–22, Nov. 2012, DOI: 10.1016/j.ndteint.2012.08.005.

[15] M. Yang, J. Zhu, Q. Liu, et al. “A practical method to calibrate the slant angle of central X-ray for laminography scanning system,” *NDT&E International*, vol. 64, pp. 13-20, Jun. 2014, DOI: 10.1016/j.ndteint.2014.02.004.

[16] W. van Aarle, W. J. Palenstijn, J. De Beenhouwer, et al. “The ASTRA Toolbox: A platform for advanced algorithm development in electron tomography,” *Ultramicroscopy*, vol. 157, pp. 35-47, May. 2015, DOI: 10.1016/j.ultramic.2015.05.002.

[17] W. Vanaarle, W. J. Palenstijn, J. Cant, et al. “Fast and flexible X-ray tomography using the ASTRA toolbox,” *Optics Express*, vol. 24, no. 22, pp. 25129-25147, 2016, DOI: 10.1364/oe.24.025129.

[18] S. Carmignato, W. Dewulf, R. Leach, “Error Sources,” in *Industrial X-Ray Computed Tomography*, Cham, Switzerland, Springer International Publishing, 2017, pp. 148.

[19] J. Lifton, A. Malcolm, J. Mcbride, et al, “The Application of Voxel Size Correction in X-Ray Computed Tomography for Dimensional Metrology,” *Singapore International NDT Conference & Exhibition*, pp. 19-20, July. 2013.

[20] Q. M. HU, M. Y. Cheng, Q. C. HE, et al, “A Preliminary of Back-projection Reconstruction Algorithm Based on Penetrating-Length Weighted for Computed Tomography,” *Chinese Journal of Medical Physics*, vol. 29, no. 2, pp. 3259-3262, Mar. 2012, DOI: 10.3969/j.issn.1005-202X.2012.02.013.

This article has been accepted for publication in a future issue of this journal, but has not been fully edited. Content may change prior to final publication. Citation information: DOI 10.1109/ACCESS.2021.3058149, IEEE Access

JIAJUN ZHANG received B.S. degree in opto-electronics information science and engineering from China University of Mining and Technology, Jiangsu, China, in 2018. He is currently pursuing the master's degree from the College of Optoelectronic Engineering , Chongqing University, Chongqing, China. His current research interests are computed tomography and geometric calibration.

LIU SHI received B.S. degree in information and computing sciences from Chongqing University, Chongqing, China, in 2019. She is currently pursuing the Ph.D. degree from the School of Nuclear Science and Technology, University of Chinese Academy of Sciences, Beijing, China. Her current research interests are particle physics and nuclear physics.

BAODONG LIU received the B.S. degree in information and computing sciences and the Ph.D. degree in instrument science and technology from Chongqing University, Chongqing, China,in 2005 and 2010, respectively. From 2011 to 2013, he was a Post-Doctoral Research Fellow with Wake Forest University. Since 2013, he has been an Associate Professor with the Institute of High Energy Physics, Chinese Academy of Sciences. He has authored/coauthored over 30 peer-reviewed journal papers. His research interests include computed tomography and image processing.

CUNFENG WEI received the B.S. degree in physics and the Ph.D. degree in condensed matter physics from Lanzhou University, Lanzhou, China,in 2001 and 2006, respectively. At present, he is a researcher and doctoral advisor with the Institute of High Energy Physics, Chinese Academy of Sciences. He is currently the director of the Division of Nuclear Technology and Applications of the Institute of High Energy Physics, Chinese Academy of Sciences. His research interests include X-ray imaging technology and equipment development.

BIAO WEI received the B.S. and Ph.D. degrees from the College of Nuclear Technology and Automation Engineering, Chengdu University of Technology, Chengdu, China, in 1988 and 1996, respectively. He held a postdoctoral position at Chongqing University, Chongqing, China, from October 1996 to May 1999. He was a Lecturer with Chongqing University from June 1999 to November 2004. He is currently a Professor and the Vice Dean of the College of Optoelectronics Engineering, Chongqing University. His research interests include optoelectronics imaging and light energy detection of X-rays, neutrons and visible light, high-resolution optoelectronics imaging detection (sensing) technology with scientific-grade CCD, EMCCD and ICCD digital camera, and optoelectronics image compression coding technology.